Journal of Biomedical Optics

BiomedicalOptics.SPIEDigitalLibrary.org

Ex vivo Mueller polarimetric imaging of the uterine cervix: a first statistical evaluation

Jean Rehbinder
Huda Haddad
Stanislas Deby
Benjamin Teig
André Nazac
Tatiana Novikova
Angelo Pierangelo
François Moreau

SPIE.

Jean Rehbinder, Huda Haddad, Stanislas Deby, Benjamin Teig, André Nazac, Tatiana Novikova, Angelo Pierangelo, François Moreau, "*Ex vivo* Mueller polarimetric imaging of the uterine cervix: a first statistical evaluation," *J. Biomed. Opt.* **21**(7), 071113 (2016), doi: 10.1117/1.JBO.21.7.071113.

Ex vivo Mueller polarimetric imaging of the uterine cervix: a first statistical evaluation

Jean Rehbinder,[a] Huda Haddad,[b] Stanislas Deby,[a] Benjamin Teig,[c] André Nazac,[d,e] Tatiana Novikova,[a] Angelo Pierangelo,[a,*] and François Moreau[a]

[a]Laboratoire de Physique des Interfaces et des Couches Minces, CNRS, Ecole polytechnique, Université Paris-Saclay, Route de Saclay, Palaiseau 91128, France
[b]Tafila Technical University, Applied Physics Department, Faculty of Science, P.O. Box 179, Tafila 66110, Jordan
[c]CHU de Bicêtre AP-HP, Service d'anatomie pathologique, 78 rue du Général Leclerc, Le Kremlin-Bicêtre 94270, France
[d]CHU de Bicêtre AP-HP, Service de Gynécologie Obstétrique, 78 rue du Général Leclerc, Le Kremlin-Bicêtre 94270, France
[e]Université Libre de Bruxelles, University Hospital Brugmann, Department of Obstetrics and Gynecology, Place A. Van Gehuchten 4, Brussels 1020, Belgium

Abstract. Early detection through screening plays a major role in reducing the impact of cervical cancer on patients. When detected before the invasive stage, precancerous lesions can be eliminated with very limited surgery. Polarimetric imaging is a potential alternative to the standard screening methods currently used. In a previous proof-of-concept study, significant contrasts have been found in polarimetric images acquired for healthy and precancerous regions of excised cervical tissue. To quantify the ability of the technique to differentiate between healthy and precancerous tissue, polarimetric images of seventeen cervical conization specimens (cone-shaped or cylindrical wedges from the uterine cervix) are compared with results from histopathological diagnoses, which is considered to be the "gold standard." The sensitivity and specificity of the technique are calculated for images acquired at wavelengths of 450, 550, and 600 nm, aiming to differentiate between high-grade cervical intraepithelial neoplasia (CIN 2-3) and healthy squamous epithelium. To do so, a sliding threshold for the scalar retardance parameter was used for the sample zones, as labeled after histological diagnosis. An optimized value of ∼83% is achieved for both sensitivity and specificity for images acquired at 450 nm and for a threshold scalar retardance value of 10.6 deg. This study paves the way for an application of polarimetry in the clinic. © *2016 Society of Photo-Optical Instrumentation Engineers (SPIE)* [DOI: 10.1117/1.JBO.21.7.071113]

Keywords: Mueller polarimetry; polarimetric imaging; cancer detection; cervical cancer.

Paper 150667SSR received Oct. 30, 2015; accepted for publication Mar. 1, 2016; published online Apr. 25, 2016.

1 Introduction

Cervical cancer continues to be a major public health issue. In the vast majority (95% to 98%) of cases, cervical cancer is due to a chronic infection by various types of human papilloma virus (HPV), especially HPV-16 and HPV-18.[1] Cervical cancer screening—primarily through the Papanicolau (Pap) test and followed, if necessary, by colposcopy—has reduced the incidence of this cancer in developed countries. However, it remains the second most common type of cancer in women worldwide due to its high incidence in low- and middle-income countries which lack the necessary resources and infrastructure to conduct regular, high-quality screening.[2] The recent introduction of vaccines against HPV[3] (which are preventive but not curative) does not eliminate the need to improve the management of this pathology in large, susceptible populations. Moreover, these vaccines do not offer full protection against all types of HPV.

After HPV infection occurs, the precancerous transformation of the cervix [cervical intraepithelial neoplasia (CIN)] starts in the cells near the basal membrane at the bottom of the squamous epithelium, and then progresses toward the surface. The lesion is classed as CIN1 or CIN2 if this transformation affects one-third or two-thirds of the epithelium thickness, respectively, and CIN3 if the entire thickness of the epithelium is affected. The disease can evolve from a high-grade dysplasia (CIN3) to an invasive cancer if the basal membrane is broken and malignant cells spread in the connective tissue underlying the epithelium. Typically, the evolution from an HPV-infected epithelium to an invasive cancer is very slow (10 to 15 years) making cervical cancer an ideal case for prevention and management by screening. The current recommendation for women with an abnormal Pap smear is a colposcopy consisting of the examination of the cervix by means of a low magnification microscope (colposcope) after successive applications of acetic acid and iodine. Areas whitened by the acetic acid and which are iodonegative are biopsied to definitively confirm the presence of a malignant transformation. The abnormal zone is surgically removed (conization) if biopsies reveal the presence of a high-grade dysplasia. Taken alone, colposcopy is strongly operator-dependent, with only 60% to 70% sensitivity and 50% specificity for CIN 2-3 detection.[4–6] Moreover, the margins of the surgical resection under colposcopy are not well-defined due to the difficulty of correctly identifying the limits of a suspicious area. A dramatic improvement in colposcopy performance is needed to make screening both more effective and less expensive. If this can be achieved, it may be incorporated as part of an economically viable "screen-and-treat" approach in low- and middle-income countries.

Several optical techniques have been explored to improve the performance of colposcopy, such as spectrally resolved

*Address all correspondence to: Angelo Pierangelo, E-mail: angelo.pierangelo@polytechnique.edu

1083-3668/2016/$25.00 © 2016 SPIE

reflectance, fluorescence imaging, *in vivo* confocal microscopy, and optical coherence tomography.[7–13] Another such technique is the polarimetric imaging, and it shows tremendous potential for biomedical applications for several reasons: (i) it exploits the polarization of light, which is sensitive to morphological changes in the structure of tissues on a microscopic scale, (ii) it is a noninvasive technique, (iii) it provides wide field images (up to 20 cm^2) for the screening of large areas, and (iv) it can be easily implemented using conventional low cost white light sources such as light-emitting diodes (LEDs) or halogen lamps. Recent studies demonstrated that polarimetric imaging is a promising technique to distinguish between healthy and pathological areas[14] on a striking variety of tissues: skin,[15] intestine,[16] colon,[17] rectum[18] and cervix.[19] In this study, the uterine cervix has been analyzed using Mueller polarimetric imaging. In previous work[19] the birefringence of tissue has been identified as one of the most relevant polarimetric parameters to detect precancerous zones on the uterine cervix. Healthy tissue displayed a strong birefringence, which was considered to be the signature of the structured and ordered collagen forming the connective tissue beneath the epithelium.[20] A precancerous evolution in the epithelium can degrade the collagen fibers in the nearby connective tissue,[21] with the consequence of a decrease in the anisotropy, and thus the birefringence of tissue.

The aim of the current work is to quantify these previously presented findings. Polarimetric images obtained for seventeen specimens of conization have been compared with the results of histological diagnoses, which is considered to be the "gold standard." In the present study, the specimens are classified according to maps of their scalar retardance values, as obtained through Mueller polarimetry. These data are then used to calculate two statistical figures of merit of the technique (sensitivity and specificity) at different acquisition wavelengths, and therefore, evaluate the performance of multispectral Mueller polarimetric imaging in distinguishing between high-grade dysplasia (CIN 2-3) and squamous healthy tissue.

The paper is structured as follows: Sec. 2 describes the collection of experimental data and the chosen statistical analysis method. In Sec. 3 the results are then presented in the form of both scalar retardance images and sensitivity and specificity curves for measurement wavelengths of 450, 550, and 600 nm. The Sec. 4 summarizes our conclusions and outlines perspectives for further development.

2 Methods

2.1 *Polarimetric Setup and Data Treatment*

The multispectral imaging Mueller polarimeter in backscattering configuration used for the *ex vivo* analysis of specimens of the uterine cervix has been described in Ref 22. For completeness, the main characteristics of the setup are recalled here. This Mueller polarimeter is based on two ferroelectric polarization modulators, and is calibrated using the eigenvalue method described in Ref. 23. A LED generating incoherent white light is used to illuminate the sample. The light impinging on the tissue is modulated by using a polarization state generator (PSG) consisting of a linear polarizer and two voltage-driven ferroelectric liquid crystals (LC). Each LC works essentially as a wave plate with fixed retardation whose fast axis orientation switches between 0 deg and 45 deg. The light backscattered by the sample is analyzed with a polarization state analyzer (PSA) which is a mirror image of the PSG, composed of the same optical elements placed in reverse order. In the detection arm, the sample is imaged through the PSA onto a charge-coupled device camera (Stingray F080B, 800×600 pixels) by means of an imaging lens (to optically "reject" the sample at infinity). A photodiode is installed in close proximity to the source to monitor the stability of the emitted light intensity during the measurement. A filter wheel in the PSA arm holds the wavelength filters, and a second wheel in the PSG arm holds the dichroic retarders used for the calibration of the polarimeter and the shutter used for the measurement of ambient light (noise). The range of wavelengths varies from 450 to 700 nm in steps of 50 nm using 40 nm wide interference filters. The choice of a broad band optical filter allows to maximize the signal to noise ratio of the detected signal and to avoid the speckle formation when using a coherent light source. The optically thick biological tissue is a highly scattering medium with the dominance of multiple scattering. Hence, the use of narrow band filter will significantly cut the intensity of the backscattered signal.

When incident spatially coherent light beam scatters on static objects the formation of the speckle pattern is observed due to the interferences. Illuminating the object with polychromatic light leads to the creation of uncorrelated patterns at different wavelengths. As there is no interference between the waves with different wavelengths, their intensities are summed incoherently, erasing speckle patterns.

Sixteen images corresponding to four different input and output polarization states are acquired to measure the Mueller matrix of the sample at each wavelength. The ferroelectric LCs used in the PSG and PSA allow rapid polarization modulation, consequently, the acquisition of these 16 images takes less than 2 s.

2.2 *Analysis of Polarimetric Images*

In this study, the Lu–Chipman algorithm[24] has been used for the polar decomposition of the measured Mueller matrix $\mathbf{M}$ into the product of three matrices for each pixel of the image

$$\mathbf{M} = \mathbf{M}_\Delta \mathbf{M}_R \mathbf{M}_D, \tag{1}$$

where $\mathbf{M}_\Delta$, $\mathbf{M}_R$, and $\mathbf{M}_D$ are the Mueller matrices of a depolarizer, a retarder, and a diattenuator, respectively. The depolarization and retardance values are found to be the important parameters for the polarimetric analysis of the uterine cervix, the diattenuation values being negligible for these samples.

The depolarization power is defined as

$$\Delta = 1 - \frac{|a| + |b| + |c|}{3}, \tag{2}$$

where a, b, and c are the eigenvalues of $\mathbf{M}_\Delta$. The scalar retardance is defined as

$$R = \cos^{-1}\left(\frac{tr(\mathbf{M}_R)}{2} - 1\right), \tag{3}$$

where $tr(\mathbf{M}_R)$ is the trace of the retarder Mueller matrix $\mathbf{M}_R$.

2.3 *Surgical Tissue Samples and Histopathological Mapping*

The current work includes a total of seventeen conization specimens obtained as part of a larger study conducted on the

Table 1 Histological types of epithelium considered in the study.

Legend	Histological type
EMS	Healthy squamous epithelium
MEM	Squamous metaplasia
EGL	Glandular epithelium
HPV	Infection (Papilloma virus)
CIN 1	Cervical Intraepithelial Neoplasia—Grade 1
CIN 2	Cervical Intraepithelial Neoplasia—Grade 2
CIN 3	Cervical Intraepithelial Neoplasia—Grade 3
OE	Endocervical canal
NOI	Non identified

premises of the University Hospital of Kremlin-Bicêtre. Patients included in the study have been scheduled for a preventive surgical excision of the uterine cervix following a standard medical procedure (e.g., after detection of abnormal cells by the Pap smear followed by detection of a high-grade lesion by colposcopy and biopsy). Occasionally surgical tissue samples were removed for other clinical purposes (total hysterectomy) providing healthy, uninfected uterine cervix specimens. Measurements on the surgical samples were performed in the department of anatomic pathology after fixation in formalin and prior to further processing by pathologists according to the conventional protocol. Fixation time was set to 24 h after reception of the fresh sample in the department.

For an accurate histopathological mapping of the precancerous lesions in the polarimetric images, a special procedure has been designed, as described in detail in Ref. 22. Before the polarimetric measurements, superficial precuts were made on the fixed sample to mark the approximate position of the future histological slides. After the polarimetric measurement, the specimen was cut along the precut lines into pieces of ~2 mm in thickness. These pieces were then enclosed in paraffin. A microtome LEICA RM2155 was used to prepare the histological slides. These slides were digitized using a commercial slide scanner LEICA Aperio CS and annotated by an expert pathologist. For this study, the epithelia were classified into one of the categories summarized in Table 1

- healthy squamous epithelium (EMS) considered to be the normal state of the cervical epithelium;
- benign epithelial modifications: glandular epithelium (EGL) usually found in the endocervical canal but which can migrate outside over the course of a woman's life, and squamous metaplasia (MEM) corresponding to the rebuilding of the squamous epithelium on the top of the EGL stimulated by the acidic environment of vagina;
- pathological epithelia subdivided into low-grade (signs of infection with the HPV, CIN1) and high-grade precancerous lesions (CIN2-3).

Once the histological slides have been interpreted and labeled, the end points of each annotated segment of epithelium are projected onto the image plane along a line as shown in the top part of Fig. 1(b). The lines, marked according to the pathologist's analysis of the slide, are then placed in the vicinity of the image of the precut line to construct a histopathological mapping of the sample [Fig. 1(a)].

Before cutting the microscopy histological slides, the trimming of thick pieces of tissue is performed with microtome. It involves the removal of the material from cross-sectional cuts of thick piece until a flat surface is obtained. This procedure leads to a 200- to 500-μm wide window of positional uncertainty for the real cut [shown as a white rectangle in Fig. 1(a)], which translates to an unavoidable uncertainty in the proper placement of the histological diagnosis lines on the polarimetric image. An equivalent uncertainty exists for the placement in vertical direction [white arrow in Fig. 1(a)].

2.4 *Histopathological Zones*

Histological mapping is used to compare the measured polarimetric contrasts (obtained from the retardance and depolarization images) to the "gold standard" diagnosis provided by the pathologist. In a previous study,[22] a statistical population of pixels corresponding to the projected marked lines was considered. This projection method suffers from two main drawbacks.

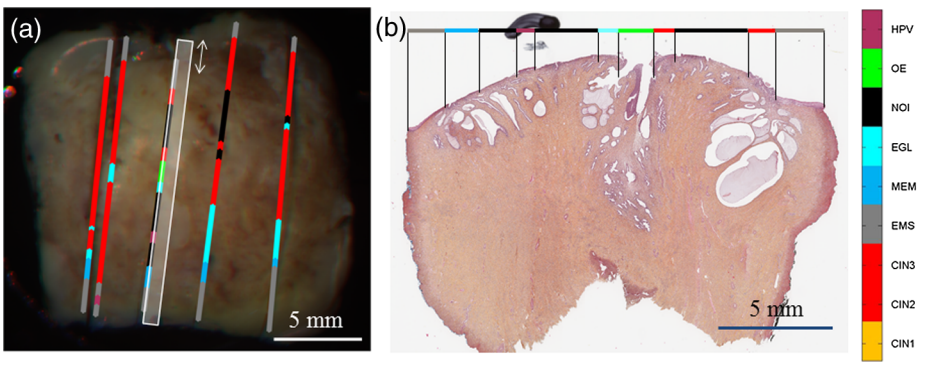

Fig. 1 Method used for the generation of a histological map. (a) Histological map (colored lines) superimposed on the image of a conization sample. (b) Histological slide corresponding to the third precut line [counted from right in (a), see text]. The projection line marked according to the pathologist's analysis of the slide is shown above the slide (for the color-code legend, see Table 1). The white box in (a) shows the uncertainty in the horizontal position of the third precut projection line. The white double arrow illustrates the uncertainty in the vertical position.

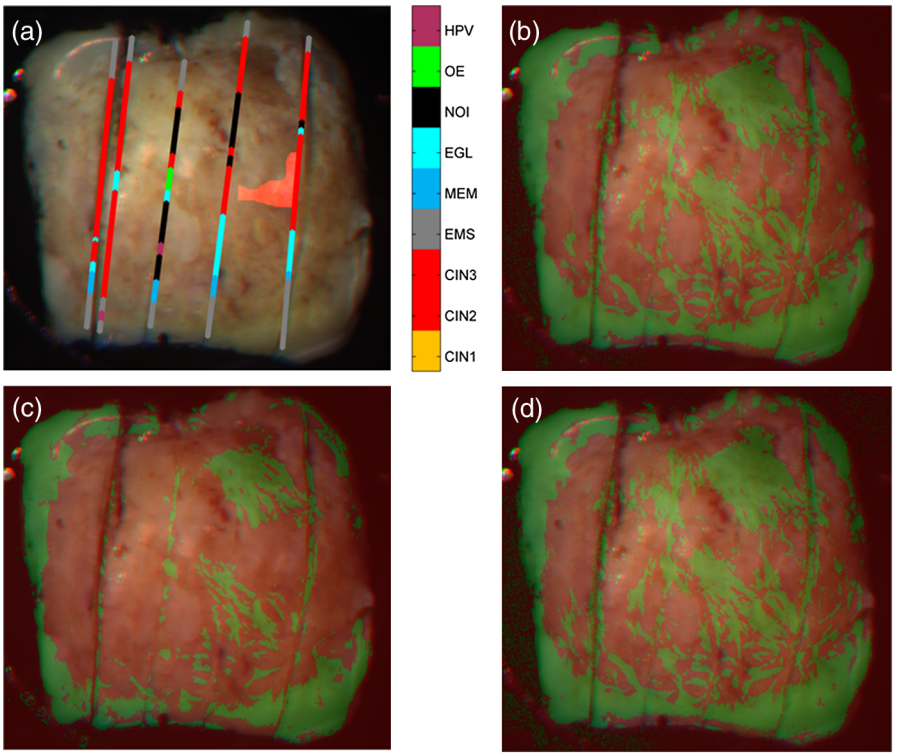

Fig. 2 (a) Example of relevant subzone on an image of conization sample. The selection of red zone is described in the text (for color-code legend refer to Table 1). (b) Image segmentation using a threshold of 8.9 deg for the scalar retardance R for measurements performed at 550 nm. (c) Image segmentation using a threshold of 10.1 deg for the scalar retardance R for measurements performed at 450 nm. (d) Image segmentation using a threshold of 9.2 deg for the scalar retardance R for measurements performed at 600 nm. Green zones of the images correspond to $R > R_{\text{threshold}}$ and red zones to $R < R_{\text{threshold}}$.

- an uncertainty in the placement of the histological lines (which can account for up to 10% variation in the final results for sensitivity and specificity). The histological slide shown in Fig. 1(b) is a good example, and demonstrates the high variability of histological diagnosis along a single epithelium cut. In this case, a small error in vertical positioning of the line can lead to a strong mismatch between the histological and polarimetric spatial diagnosis;
- an uncertainty linked with the projection procedure. The orientation of the histological cut with respect to the image plane is not well known, especially for slides consisting of two separated parts (when the cut goes through the endocervical canal).

In order to avoid these systematic effects, another method of the statistical evaluation is implemented in this study. It consists of selecting subzones of the polarimetric image between two adjacent lines marked by the same histological diagnosis. Figure 2(a) gives an example of one such selected zone (marked in red), located between the corresponding parts of the adjacent lines having the same CIN3 annotation. It is then assumed that with a high degree of certainty there is no variation of the histological type of epithelium in the selected subzone.

3 Results and Discussion

It is known that CIN3 lesions are considered as the life threatening conditions which require a surgical intervention, while for low grade CIN1 lesions, watchful waiting is often the best strategy. That is why in this study we only attempt to distinguish between the polarimetric response of healthy tissue (EMS) and high-grade neoplasia CIN 2-3, expecting the high grade lesions to have a stronger polarimetric contrast. For the moment, we do not include in the analysis the areas containing benign epithelia (MEM and EGL), HPV-infected epithelia, or low-grade dysplasia CIN1.

Our preliminary studies[19] performed on fresh conization specimens showed that for binary (healthy-CIN3) classification the tissue scalar retardance R is the most relevant parameter. Simultaneously, the subtle staging of neoplastic lesions as well as the discrimination of some benign lesions is rather related to the tissue depolarization power Δ [e.g., $\Delta(\text{CIN3}) < \Delta(\text{CIN2}) < \Delta(\text{CIN1}) < \Delta$ (healthy squamous epithelium)]. It was reported that tissue fixation in formalin increases the light scattering and, consequently, the depolarization of light backscattered by tissue.[25] That is why we did not use the parameter Δ (depolarization power) for CIN staging and focused our studies on binary image segmentation.

To compute sensitivity and specificity, the statistical population of pixels is provided by subzones selected as described in Sec. 2.4. The polarimetric diagnosis map is calculated using the scalar retardance R images in the following way: in a precancerous subzone, pixels with R value lower than the threshold are considered as true positives (TP), while in a healthy region, pixels with a R value higher than the threshold are considered as true negative (TN). False positive (FP) pixels are those which were identified as diseased by polarimetric analysis

($R < R_{\text{threshold}}$), but were labeled as healthy by histological diagnosis. False negative pixels (FN) are those which were considered healthy by polarimetric analysis ($R > R_{\text{threshold}}$) but were tagged as CIN3 by histological diagnosis. Sensitivity and specificity are then obtained according to the Eqs. (4) and (5):

$$\text{Se} = \frac{\text{TP}}{\text{TP} + \text{FN}}, \tag{4}$$

$$\text{Sp} = \frac{\text{TN}}{\text{TN} + \text{FP}}. \tag{5}$$

The total number of pixels included in the analyzed zones is slightly over 163,000, of which about 35,000 were labeled as CIN2-3 and 128,000 as healthy by histological analysis. For this sample set of pixels, each clearly associated with a histopathological diagnosis, the accuracy of the polarimetric imaging diagnostic technique is optimized by applying a sliding threshold to the R values when classifying the pixels.

Figures 2(b)–2(d) show the polarimetric diagnostic binary segmentation of the conization sample image shown in Fig. 2(a) for the threshold values of $R_{\text{threshold}} = 8.9$ deg at wavelength 550 nm, $R_{\text{threshold}} = 10.1$ deg at wavelength 450 nm, and $R_{\text{threshold}} = 9.2$ deg at wavelength 600 nm, respectively. Pixels with scalar retardance values above and below the threshold are highlighted in green and red, respectively.

The segmentation of the retardance R image taken at 550 nm [Fig. 2(b)] is very similar to that of the retardance image taken at 600 nm [Fig. 2(d)]. The red zone marked as the diseased one (CIN 3) on the retardance image taken at 450 nm [Fig. 2(c)] visually occupies larger area compared to the images taken at 550 and 600 nm. We attribute this effect to the different

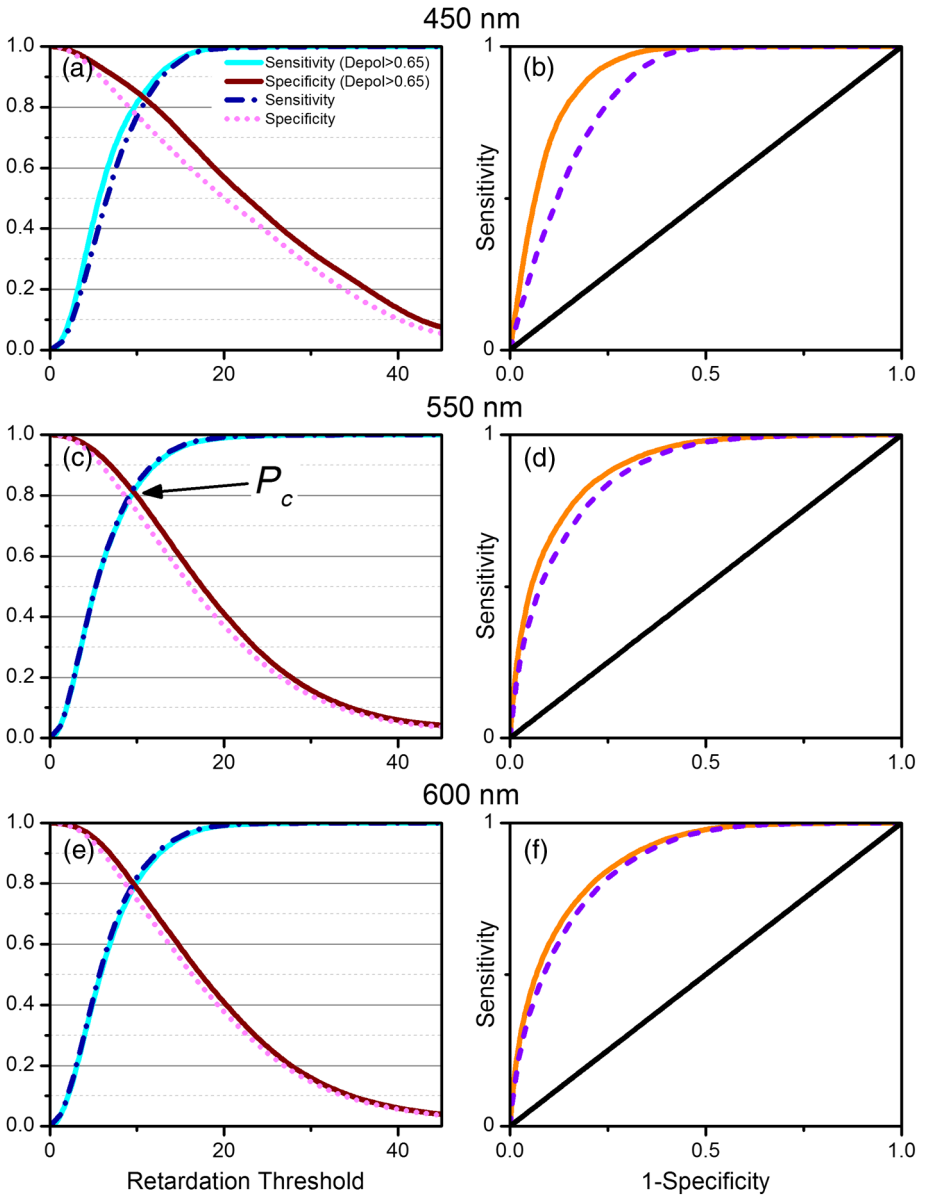

Fig. 3 Classification outcome statistics when varying $R_{\text{threshold}}$: (a), (c), and (e) sensitivity (dash-dotted blue) and specificity (dotted magenta) curves. Cyan and brown solid lines correspond to statistics corrected for specular reflections. Pc is the crossing point of the Se and Sp curves. (b), (d), and (f) resulting ROC curves (dashed violet lines for the initial statistics and orange lines for statistics corrected for specular reflections) as compared with the Se = 1-Sp line (black solid line), corresponding to a random test.

Table 2 Statistical performance of the polarimetric classification based on R value (R_{th}: threshold, Se: sensitivity, and Sp: specificity).

	450 nm			550 nm			600 nm		
	R_{th}	Se	Sp	R_{th}	Se	Sp	R_{th}	Se	Sp
All pixels	10.1°	77.6%	77.1%	8.9 deg	78.7%	78.8%	9.2 deg	78.1%	77.8%
($\Delta > 0.65$)	10.6°	83.8%	83.6%	9.7 deg	81.7%	80.9%	9.8 deg	79.7%	79.2%

Table 3 Area under the curve and Youden indices for the ROC curves presented in Fig. 3.

	450 nm		550 nm		600 nm	
	All pixels	($\Delta > 0.65$)	All pixels	($\Delta > 0.65$)	All pixels	($\Delta > 0.65$)
AUC	0.85	0.91	0.87	0.89	0.86	0.88
Max. Youden index (associated R_{th} value)	0.59 (13.2 deg)	0.70 (13.0 deg)	0.59 (10.3 deg)	0.63 (10.4 deg)	0.57 (10.6 deg)	0.59 (10.6 deg)

penetration depth of the probing light. The mole extinction coefficient of hemoglobin, which is the main source of light absorption in tissue, drops with the increase of measurement wavelength. Therefore, at longer wavelengths we collect the light which penetrates deeper and the impact of underlying layers on the detected signal becomes dominant. The spectral dependence of the segmentation will also help to stage the lesions: superficial versus locally advanced ones.

To determine the optimum retardance threshold for separating healthy and CIN2-3 regions, both sensitivity and specificity curves were calculated as a function of the threshold. Figures 3(a), 3(c), and 3(e) show such curves for three different measurement wavelengths: 450, 550, and 600 nm, respectively.

For low threshold values, all "healthy" pixels are correctly classified, leading to a low false positive rate (specificity is near unity), but many CIN2-3 pixels may be misclassified, leading to a high false negative rate (sensitivity is near zero). In contrast, an overly high threshold value results in low specificity and high sensitivity values. The crossing point (P_c) of the two curves provides an optimal performance threshold, balancing both metrics [see Figs. 3(a), 3(c), and 3(e)]. For example, at 550 nm, a $R_{\text{threshold}}$ value of 8.9 deg leads to 78.7% of both sensitivity and specificity.

The statistical accuracy of the technique is improved by removing from sampling any pixels with a significant contribution of specular reflection, which masks the contribution of volume light scattering to the measurement of polarimetric parameters. These pixels can be identified with a high degree of confidence by using the depolarization power parameter Δ from the Lu–Chipman polar decomposition. Indeed, specular reflection adds a completely polarized component to the light backscattered by the tissue, thus lowering the depolarization power Δ value. Typical values of Δ —as observed in 17 fixed conization samples—vary between 0.65 and 0.9. We, therefore, assume that pixels having a depolarization power $\Delta < 0.65$ are "contaminated" by some specular reflection, and then we removed them from the initial statistical sample.

The results at the point P_c obtained for the sampling with and without the pixels affected by the specular reflection are summarized in Table 2 for three measurement wavelengths.

It can be seen that the classification performance is improved when removing the pixels affected by specular reflection. The best performance is achieved at $\lambda = 450$ nm, with values of more than 83% for both sensitivity and specificity.

This statistical performance can also be displayed by a receiver operating characteristic (ROC) curve, as shown for each wavelength in Figs. 3(b), 3(d), and 3(f). This curve allows one to compare the performance from different classifiers and is commonly used to assess the quality of a diagnostic test. The ROC curve shows Se values as a function of 1-Sp values. The line with equation Se = 1-Sp shows the performance of a perfectly random test. Different criteria can be extracted from ROC curve in order to choose the best classifier depending on the purpose. For example, the area under the curve (AUC) is often used as a simple metric to compare classifiers on the whole range of sensitivity and specificity values while the Youden index[26] gives the best achievable compromise between sensitivity and specificity for a given classifier. The Youden index is equal to Se + Sp−1 and represents the distance between the test ROC curve and the random test line in the ROC space.

Taking both the AUC and the maximal Youden index as performance indicators for the classification test, we obtain the data shown in Table 3 for the different measurement wavelengths.

In our case, the evolution of AUC parameter with wavelength provides a global vision of the test performance compared with the evolution of punctual values of Sp and Se at P_C. We find the same trend as before: the best performance is obtained at 450 nm but the influence of specular reflections is also bigger at this wavelength. In a medical setting, the classifier will be implemented at a particular, previously chosen, threshold value. The Youden index is the best to evaluate this optimal value. We see that the threshold values of R (shown in Table 3) are slightly higher than the corresponding values for P_C. The gain in sensitivity is higher than the loss of specificity while changing the threshold between the two values. For example,

at 450 nm we obtain the values of Se = 92.0% and Sp = 77.6% calculated with $R_{\text{threshold}} = 13.0$ deg for the set of image pixels with $\Delta > 0.65$.

The ROC curve is a benchmarking tool independent of the choice of the classification parameter. Using normalized values obtained on the basis of the ROC curves, the rather simple thresholding approach presented here can be compared, in the future, with more complex classification algorithms which combine several polarimetric parameters.

4 Conclusions

In this work, polarimetric imaging has been used to obtain maps of the scalar retardance of the uterine cervix, and the effectiveness of using such maps to distinguish precancerous zones of high-grade CIN2-3 from healthy EMS zones has been statistically evaluated. For 17 studied fixed conization samples, an averaged value of both sensitivity and specificity of 83% have been achieved at a measurement wavelength of 450 nm (after the elimination of the contribution of specular reflections) using the scalar retardance parameter value obtained from Lu–Chipman decomposition.

The best performance of the proposed optical technique in terms of sensitivity and specificity [Eqs. (4) and (5)] is obtained at shorter wavelengths because the precancerous transformations of epithelium affect first the collagen layer restricted to a shallow area underneath the epithelium ($\sim 300 - 500\,\mu$m).[20,21] The further modifications of deeper tissue layers can be taken into account when probing the sample with larger wavelengths of the light.

A single optimum threshold value of $R_{\text{threshold}} = 10.6$ deg has been found for all analyzed samples when sampling the pixels belonging to areas between two adjacent histological slides that possess the same histological diagnosis.

These results allow one to evaluate the technique itself, as well as to understand the limits of Mueller polarimetric imaging as a diagnostic tool. The characterization of the polarimetric signature of benign alterations (metaplasia MEM and glandular EGL) and low-grade precancerous lesions (CIN1), must be done as a future refinement of the technique. For *in vivo* applications of our optical technique the analysis of both scalar retardance and depolarization power values[17,27] may provide the necessary information for both cervical cancer diagnosis and staging.

Notwithstanding these remaining challenges, the Mueller matrix polarimetric imaging technique has been shown to be quantifiably effective in accurately distinguishing between healthy and diseased zones of the uterine cervix. Furthermore, it has done so using a fast wide field noninvasive imaging method, making it a promising future tool for the early detection of cervical cancer.

Acknowledgments

The authors would like to pay the tribute to the seminal ideas of our group leader Dr. Antonello De Martino who passed away in August 2014. He pioneered the biomedical applications of Mueller polarimetry. This work was funded by the "Institut National du Cancer (INCa)" and the "Cancéropôle," under contract #2012-1-GYN-01-EP-1. The authors would like to thank the technical staff of the Department of Anatomic Pathology of the Kremlin Bicêtre University hospital. The authors would also like to thank Frederic Farci and Jean Charles Vanel for the technical support.

References

1. D. R. Lowy et al., "Human papilloma virus infection and the primary and secondary prevention of cervical cancer," *Cancer* **113**(7 Suppl), 1980–1993 (2008).
2. J. Ferlay et al., "Estimates of worldwide burden of cancer in 2008: GLOBOCAN 2008," *Int. J. Cancer* **127**(12), 2893–2917 (2010).
3. M. Drolet et al., "Population-level impact and herd effects following human papilloma virus vaccination programmes: a systematic review and meta-analysis," *Lancet Infect Dis.* **15**(5), 565–580 (2015).
4. M. Underwood et al., "Accuracy of colposcopy-directed punch biopsies: a systematic review and meta-analysis," *BJOG* **119**(11), 1293–1301 (2012).
5. L. S. Massad and Y. C. Collins, "Strength of correlations between colposcopic impression and biopsy histology," *Gynecol. Oncol.* **89**(3), 424–428 (2003).
6. S. B. Cantor et al., "Accuracy of colposcopy in the diagnostic setting compared with the screening setting," *Obstet. Gynecol.* **111**(1), 7–14 (2008).
7. I. M. Orfanoudaki, D. Kappou, and S. Sifakis, "Recent advances in optical imaging for cervical cancer detection," *Arch. Gynecol. Obstet.* **284**(5), 1197–1208 (2011).
8. N. Thekkek and R. Richards-Kortum, "Optical imaging for cervical cancer detection: solutions for a continuing global problem," *Nat. Rev. Cancer* **8**(9), 725–731 (2008).
9. R. D. Alvarez and T. C. Wright Jr., and Optical Detection Group, "Increased detection of high-grade cervical intraepithelial neoplasia utilizing an optical detection system as an adjunct to colposcopy," *Gynecol. Oncol.* **106**(1), 23–28 (2007).
10. R. D. Alvarez and T. C. Wright, and Optical Detection Group, "Effective cervical neoplasia detection with a novel optical detection system: a randomized trial," *Gynecol. Oncol.* **104**(2), 281–289 (2007).
11. M. Cardenas-Turanzas et al., "The clinical effectiveness of optical spectroscopy for the in vivo diagnosis of cervical intraepithelial neoplasia: where are we?" *Gynecol. Oncol.* **107**(1 Suppl. 1), S138–S146 (2007).
12. T. DeSantis et al., "Spectroscopic imaging as a triage test for cervical disease: a prospective multicenter clinical trial," *J. Low. Genit. Tract Dis.* **11**(1), 18–24 (2007).
13. R. A. Drezek et al., "Laser scanning confocal microscopy of cervical tissue before and after application of acetic acid," *Am. J. Obstet. Gynecol.* **182**(5), 1135–1139 (2000).
14. N. Ghosh and A. Vitkin, "Tissue polarimetry: concepts, challenges, applications, and outlook," *J. Biomed. Opt.* **16**(11), 110801 (2011).
15. S. L. Jacques, J. C. Ramella-Roman, and K. Lee, "Imaging skin pathology with polarized light," *J. Biomed. Opt.* **7**(3), 329–340 (2002).
16. W. Wang et al., "Investigation on the potential of Mueller matrix imaging for digital staining," *J. Biophotonics* **9999** (2015).
17. A. Pierangelo et al., "Ex-vivo characterization of human colon cancer by Mueller polarimetric imaging," *Opt. Express* **19**(2), 1582–1593 (2011).
18. A. Pierangelo et al., "Multi-spectral Mueller polarimetric imaging detecting residual cancer and cancer regression after neoadjuvant treatment for colorectal carcinomas," *J. Biomed. Opt.* **18**(4), 046014 (2013).
19. A. Pierangelo et al., "Polarimetric imaging of uterine cervix: a case study," *Opt. Express* **21**(12), 14120–14130 (2013).
20. S. Bancelin et al., "Determination of collagen fiber orientation in histological slides using Mueller microscopy and validation by second harmonic generation imaging," *Opt. Express* **22**(19), 022561 (2014).
21. A. Nazac, "Imagerie polarimétrique pour le diagnostic du cancer du col uterin: etude de conisations et de lames histologiques de tissue conjonctifs," PhD thesis, Ecole Polytechnique (2013).
22. J. Rehbinder et al., "Diagnosis of uterine cervix cancer using Müller polarimetry: a comparison with histopathology," *Proc. SPIE* **9540**, 95400W (2015).
23. B. Laude-Boulesteix et al., "Mueller polarimetric imaging system with liquid crystals," *Appl. Opt.* **43**(14), 2824–2832 (2004).
24. S. Y. Lu and R. A. Chipman, "Interpretation of Mueller matrices based on polar decomposition," *J. Opt. Soc. Am. A* **13**(5), 1106–1113 (1996).
25. M.F. Wood et al., "Effects of formalin fixation on tissue optical polarization properties," *Phys. Med. Biol.* **56**(8), N115–N122 (2011).
26. W. J. Youden, "Index for rating diagnostic tests," *Cancer* **3**, 32–35 (1950).
27. T. Novikova et al., "The origins of polarimetric image contrast between healthy and cancerous human colon tissue," *Appl. Phys. Lett.* **102**, 241103 (2013).

Jean Rehbinder is an alumnus of Ecole Polytechnique (France), ESPCI (France) and holds a PhD of the University of Heidelberg, Germany. His PhD work was devoted to non-linear microscopy with shaped femtosecond pulses. Since then, he works as a postdoctoral researcher at Ecole Polytechnique on polarimetric imaging for the cancer detection.

Huda Haddad: Biography is not available.

Stanislas Deby has obtained his master's degree in engineering (valedictorian) at University Paris-Saclay (made by apprenticeship in the LPICM, École polytechnique) and his MBA at IAE-de-Paris. During his engineering degree he worked on a biomedical project to improve the detection of cervical cancer. Today, he is a PhD candidate at École polytechnique. The topic of his thesis is the evaluation of polarimetric imaging for monitoring of chemo-radiotherapy in the treatment of cervical cancers.

Benjamin Teig graduated from Paris Medical School in 2006 and specialized in pathology over a 5-year residency and a fellowship in Paris, with a teaching appointment at Paris-Sud teaching hospital. He is now working as a fully qualified pathologist with the Paris Hospitals (AP-HP, Paris, France) and focuses on the feminine genital tract pathohistology and the implementation of new tools and assays for the early detection of cervical cancer.

André Nazac is a gynecologic surgeon and obstetrician. He also earned his PhD in physics from the Ecole polytechnique in 2013, with a work targeting the anatomic structures at the origin of polarimetric contrast in cervical tissue. He is currently appointed as chief of gynecology surgery department at Brugmann Hospital (Belgium) and is member of various scientific societies, including the French Society of Colposcopy, since 2008.

Tatiana Novikova is a researcher at the Applied Optics and Polarimetry group of the Laboratory of Interfaces and Thin Films, Ecole Polytechnique, France. She received her MS degree (cum laude) in applied mathematics from Moscow State University, Russia, PhD degree in applied physics and mathematics from Moscow Institute of Mathematical Modeling, Russian Academy of Sciences, and HDR (habilitation) in physics from Paris-Sud University, Orsay, France. Her current research interests focus on polarized light interaction with different media, including numerical modeling and practical applications of Mueller polarimetry to the problems of metrology for the semiconductor industry, target detection, and polarimetric imaging for biomedical applications.

Angelo Pierangelo received the Laurea Degree in physics in 2004 at the University of L'Aquila in Italy. In 2007 he completed his PhD in electromagnetism at the University of Rome, La Sapienza in the domain of Non linear Optics. After 2008 he joined the Laboratoire de Physique des Interfaces et des Couches Minces (LPICM) in Paris to work on polarimetric imaging for biomedical applications. He currently leads the biomedical research activities at LPICM.

François Moreau is a research director at CNRS and has joined the polarimetric imaging team since 3 years. He spent a large part of his career in particle physics, during which he developed several calorimetric detectors and their associated front-ends electronics.